Title
Thermal evidence for Taylor columns in turbulent rotating Rayleigh-Bénard convection

Journal
Physical Review E, 85(1)

ISSN
2470-0045

Authors
King, Eric M
Aurnou, Jonathan M

Publication Date
2012

DOI
10.1103/physreve.85.016313

Peer reviewed

Thermal evidence for Taylor columns in turbulent rotating Rayleigh-Bénard convection

Eric M. King
Department of Earth and Planetary Science, University of California, Berkeley, California 94720, USA

Jonathan M. Aurnou
Department of Earth and Space Sciences, University of California, Los Angeles, California 90095, USA

(Received 4 May 2011; revised manuscript received 8 September 2011; published 18 January 2012)

We investigate flow structures in rotating Rayleigh-Bénard convection experiments in water using thermal measurements. We focus on correlations between time series measurements of temperature in the top and bottom boundaries. Distinct anticorrelations are observed for rapidly rotating convection, which are argued to attest to heat transport by convective Taylor columns. In support of this argument, these quasigeostrophic flow structures are directly observed in flow visualizations, and their thermal signature is qualitatively reproduced by a simple model of heat transport by columnar flow. Weakly rotating and nonrotating convection produces positively correlated temperature changes across the layer, indicative of heat transport by large-scale circulation. We separate these regimes using a transition parameter that depends on the Rayleigh and Ekman numbers, $\mathrm{Ra}E^{3/2}$.

DOI: 10.1103/PhysRevE.85.016313 PACS number(s): 47.32.C−, 47.55.P−

I. INTRODUCTION

Fluid motions in planetary systems are subject to Coriolis forces resulting from the planet's rotation. A strong Coriolis force imposes an organizational influence on otherwise turbulent flow that is thought to be responsible for, *inter alia*, the alignment of Earth's rotation axis and magnetic dipole. Here, we examine results from a simple experimental analog of such planetary fluid systems: rotating Rayleigh-Bénard convection.

Rayleigh-Bénard convection (RBC) is a horizontal layer of fluid through which heat is fluxed from bottom to top. Fluid near the bottom boundary is warmed, expands, and rises due to gravitational instability. Rotating RBC has an identical setup, but fluid and boundaries spin about a vertical axis. Many planetary convection systems are considered rapidly rotating, meaning that the period of rotation is among the fastest dynamical time scales present. Rapidly rotating flows are typically described by the so–called geostrophic force balance, a balance between the Coriolis force and pressure gradient. The curl of this force balance produces the Taylor–Proudman theorem [1]:

$$\Omega\hat{\mathbf{z}} \cdot \nabla \mathbf{u} = 0, \tag{1}$$

where $\Omega\hat{\mathbf{z}}$ and $\mathbf{u}$ are the rotation and flow vectors, respectively. Although convective flow cannot strictly abide by this constraint beyond the lowest order, a strong Coriolis force nevertheless tends to align flow with the axis of rotation in what is considered quasigeostrophic convection.

Flow in quasigeostrophic RBC is manifest as a vortex grid of so-called convective Taylor columns (CTCs) [e.g., [2]]. A CTC is a helical vortex with either upward or downward flow [3]. The sign of vorticity ($\boldsymbol{\omega} \equiv \nabla \times \mathbf{u}$) in an upward flowing CTC is positive in the lower half of the layer ($z < h/2$) and negative in the upper half ($z > h/2$). Conversely, a downward flowing CTC will have negative vorticity in the lower half of the layer and positive vorticity in the upper half. For both upward and downward flowing CTCs, then, helicity ($\mathbf{u} \cdot \boldsymbol{\omega}$) is positive in the lower half and negative in the upper half. A schematic depiction of CTCs is shown in Fig. 1(a).

For rapidly rotating convection, roughly equal numbers of upward and downward flowing CTCs are expected [4]. Vortex-vortex interactions between the CTCs cause them to be advected laterally about the container [e.g., [5]]. This horizontal "dance" of the axial CTCs has been observed in movies of quasigeostrophic RBC in experiments [6] and numerical simulations [4,7].

If a convection system rotates slowly enough or if the vigor of convection is strong enough, inertial forces can overwhelm the Coriolis force, resulting in weakly rotating convection, which behaves similarly to nonrotating convection. Experimental work [e.g., [8,9]] has seen the development of large-scale circulation in weakly rotating convection like those typical of nonrotating RBC experiments [e.g., [10,11]]. This large-scale circulation results from the interaction of nonlinear entrainment processes and the experimental convection tank geometry [12]. Figure 1(b) shows a schematic depiction of the flywheel pattern of a large-scale circulation.

The different regimes of rotating convection are often examined using heat transfer measurements in experiments and simulations to distinguish competing influences of buoyancy and rotation [e.g., [7,13–20]]. Some work, however, is able to connect flow and heat transfer regimes. References [21,22], for example, measure heat transfer efficiency and helicity in rotating RBC simulations, showing that heat transfer and flow structure regimes are linked by a relationship that depends only on the Prandtl number. Experimentally, it is difficult to simultaneously characterize flow patterns and heat transfer, as visualization techniques can compromise thermal control [e.g., [23]]. Here, we measure temporal correlations of thermal signals to infer large-scale patterns of convection in rotating RBC experiments. For quasigeostrophic convection, in particular, we may expect that the random horizontal dance of the CTCs should produce significant thermal anomalies nearly simultaneously on stationary, vertically aligned temperature probes.

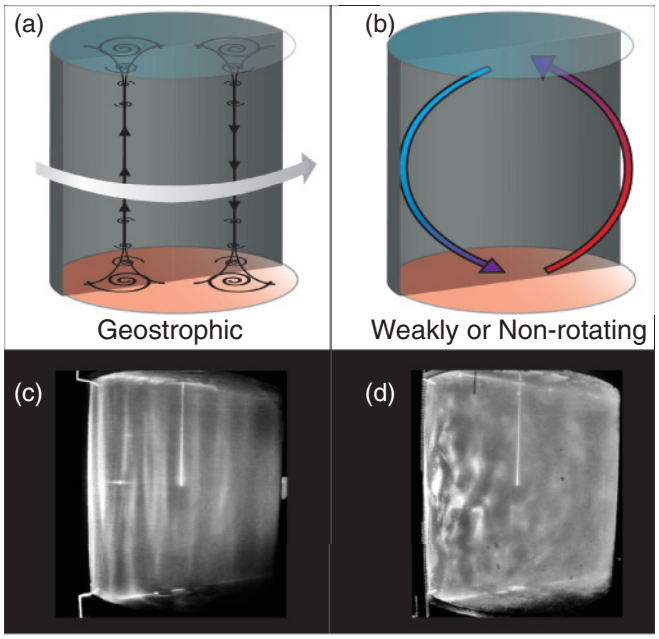

FIG. 1. (Color online) Flow regimes in rotating RBC. (a) An illustration of two CTCs in quasigeostrophic convection. (b) An illustration of a large-scale circulation typical of turbulent weakly or nonrotating RBC. (c and d) Visualizations of flow regimes in rotating RBC experiments. A vertical sheet of laser light is projected through the center of a 20-cm-tall, uninsulated convection tank. Both panels show convection in water (plus trace amounts of Kalliroscope particles) driven by 100 W of heating power and rotated at 4.3 Hz (c) and 0.43 Hz (d). Approximate nondimensional parameters are then Pr$\approx$ 7, $R_f \approx 1.1 \times 10^{11}$, $E \approx 3 \times 10^{-6}$ (c), and $E \approx 3 \times 10^{-5}$ (d).

II. METHOD

A. Experiments

We conduct rotating convection experiments in water (Pr $\approx$ 7) and sucrose solution (Pr $\approx$ 10) using the rotating magnetoconvection device at University of California, Los Angeles. Figure 2 shows a schematic depiction of the experimental setup. The convection tank is a 20-cm-diameter cylinder whose top and bottom end walls are 4-cm-thick aluminum and 1.3-cm-thick copper blocks, respectively. The fluid is contained by polycarbonate sidewalls with heights varying between 3.2 and 19.7 cm. An electrical heating element is mechanically fixed to the bottom of the lower end wall. Between 5 and 600 W of heat is passed through the end walls and fluid and is removed above the upper end wall by thermostated water flowing through an aluminum heat exchanger, which is isothermal to within 0.05 K. The convection tank setup is insulated by closed cell foam, 20-cm thick, to minimize heat losses through the sidewalls. The experimental apparatus (convection tank setup and diagnostic systems) is rotated up to fifty revolutions per minute (5.2 Hz). More detailed descriptions of the device and experimental method can be found in [24,25].

We report results from a suite of 64 rotating and 12 nonrotating convection experiments. These experiments represent a subset of those presented in [7,25]. Time series from each experiment have at least 25 000 data points, acquired at 10 Hz for at least 45 min. The control parameters fixed experimentally are tank height h, rotation rate Ω, input heat power Q, as well as fluid properties. The nondimensional parameters fixed for each convection experiment are the Prandtl number Pr, Ekman number E, flux Rayleigh number R_f, and the tank diameter-to-height aspect ratio Γ. Table I defines these and other relevant experimental parameters. In this study, we focus on changes in dynamics as R_f and E vary over several orders of magnitude.

Figures 1(c) and 1(d) show frames from video taken in a complementary set of experiments for qualitative visualization. Here, the insulation is removed from the sidewall of the convection tank, and Kalliroscope particles in water are illuminated by a vertical sheet of laser light projected through the center of the tank [e.g., [26]]. Such visualizations allow us to check more directly the existence of CTCs that are indirectly observed using temperature time series measurements in thermally insulated experiments.

The prime diagnostic of interest here is temperature time series measurements. We use these measurements to distinguish the two flow regimes depicted in Fig. 1. To accomplish this goal, we place six thermistors within the solid bottom end wall, 2 mm below the fluid, and another six thermistors within the solid top end wall, 2 mm above the fluid [see Fig. 2(a)]. The probes are arranged to form six vertically aligned pairs, equally spaced in azimuth [see Fig. 2(b)]. Figure 3 shows an example of temperature time series measurements from a thermistor within each of the top and bottom end walls. These temperature measurements are denoted $T_i^{\text{top}}(t)$ and $T_i^{\text{bottom}}(t)$, where $i = 1,\ldots,6$, corresponding to azimuthal location [see Fig. 2(b)]. The temperature cross correlation is calculated using temperature time series measurements of top and bottom thermistors at the same location in azimuth:

$$C_i^{\text{top-bottom}}(m) = \sum_{t/dt=0}^{N-|m|-1} \left[T_i^{\text{top}}(t) - \left\langle T_i^{\text{top}}(t)\right\rangle_t\right] \times \left[T_i^{\text{bottom}}(t + m\,dt) - \left\langle T_i^{\text{bottom}}(t)\right\rangle_t\right], \quad (2)$$

where t is the measurement time and dt is the inverse of the data-acquisition frequency such that $t/dt = 0,1,\ldots,N$, where N is the total number of data points acquired in time and integers $m = 1-2N,\ldots,2N-1$ represent the correlation lag. $C_i(m)$ is then normalized such that the autocorrelation at zero lag, $C_i^{\text{top-top}}(m=0)$, is unity.

The mean, zero-lag correlation of the six pairs can be calculated such that a single correlation coefficient is produced for each convection experiment:

$$\overline{C} = \frac{1}{6}\sum_{i=1}^{6} C_i^{\text{top-bottom}}(m=0). \quad (3)$$

This quantity allows us to gauge the nature of flow structures as a function of our changing parameters for all 76 experiments conducted.

III. RESULTS

Figure 1 shows visualizations of quasigeostrophic (panel c) and weakly rotating (panel d) convection in uninsulated experiments. We quantify the relative influence of rotation and

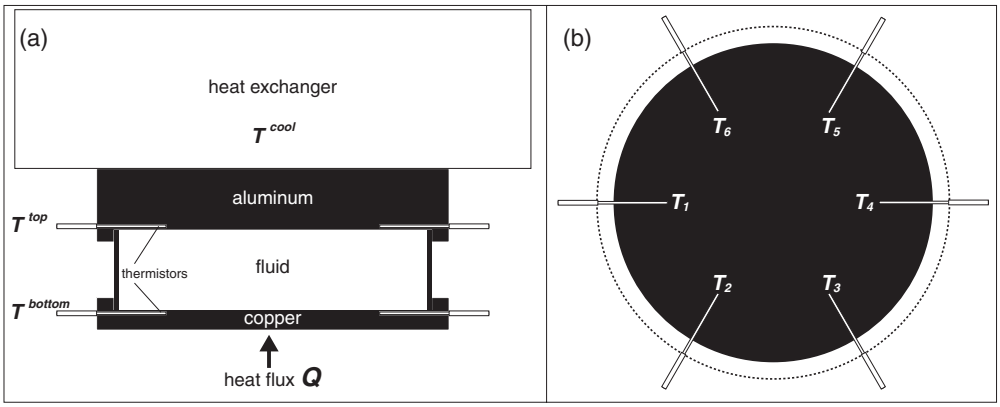

FIG. 2. A scaled illustration of the experimental apparatus. (a) A side view showing the vertical structure of the tank setup with a 5-cm sidewall. T^{top} and T^{bottom} show the vertical locations of the top and bottom thermistors. (b) A plan view of the convection tank setup showing the horizontal orientation of the top and bottom thermistor pairs, $T_{1,\ldots,6}$.

buoyancy using the transition parameter of [25]. The transition between quasigeostrophic and weakly rotating convection regimes is argued to be controlled by the relative thicknesses of the thermal and Ekman boundary layers [7], and the ratio of their thicknesses can be characterized by a transition parameter $\text{Ra}E^{3/2}$. We show in [25] that the thermal boundary layer becomes thinner than the Ekman boundary layers when $\text{Ra}E^{3/2} \gtrsim 20$, which coincides with a transition from quasigeostrophic to weakly rotating heat transfer behavior. The quasigeostrophic experiment shown in Fig. 1(c) has $\text{Ra}E^{3/2} \approx 8$, and the weakly rotating experiment shown in panel (d) has $\text{Ra}E^{3/2} \approx 280$. The former experiment reveals the existence of container-high CTCs in the more rapidly rotating case (c), which, in order to expose the fluid for visualization, are not well controlled thermally.

Figures 4(a) and 4(b) show measurements of $C_i^{\text{top-bottom}}$ from quasigeostrophic convection experiments for each of the six thermistor pairs ($i = 1, \ldots, 6$). Panel (a) has $R_f = 2 \times 10^8$, and $E = 4.4 \times 10^{-5}$. Panel (b) has $R_f = 1.1 \times 10^{11}$, and $E = 3 \times 10^{-6}$ [identical to the experiments shown in Fig. 1(c)]. These convection experiments are considered quasigeostrophic, as they have $\text{Ra}E^{3/2} \approx 5$ and $\text{Ra}E^{3/2} \approx 8$, respectively, and transport heat less efficiently than nonrotating but are otherwise identical experiments (by 30% and 10%, respectively). The instantaneous ($m = 0$) thermal variations are vertically anticorrelated.

The *anti*-correlation of these quasigeostrophic temperature signals is perhaps counterintuitive. Upward flowing CTCs transport warm material from the bottom boundary to the top, and downward flowing columns bring cold material from top to bottom. The CTCs are then either anomalously hot or cold, and measurements of temperature on vertical pairs of thermistors within the fluid should exhibit positive correlations. Our measurements, however, are taken in the tank's end wall, not in the fluid, and this difference is important in producing the anticorrelated thermal signals. Convective heat transfer can be parameterized locally as $\mathbf{u}T'$, where T' is the local temperature anomaly [e.g., [27]]. Both warm, upward flowing,

TABLE I. Relevant experimental parameters.

Parameter	Definition	Experiments
	Dimensional	
h	Tank height	$0.032 \leqslant h \leqslant 0.197$ m
Q	Heat power	$5 \leqslant Q \leqslant 600$ W
Ω	Rotation rate	$0 \leqslant \Omega \leqslant 5.2$ Hz
ν	Viscous diffusivity	$7.2 \times 10^{-7} \leqslant \nu \leqslant 1.5 \times 10^{-6}$ m^2/s
κ	Thermal diffusivity	1.4×10^{-5} m^2/s
α_T	Thermal expansivity	$0.002 \leqslant \alpha_T \leqslant 0.0043$ K^{-1}
k	Thermal conductivity	0.6 W/mK
A	Cross-sectional area	0.0314 m^2
ΔT	Temperature difference	$2.2 \leqslant \Delta T \leqslant 45$ K
	Dimensionless	
Aspect ratio	$\Gamma \equiv [4A/(\pi h^2)]^{1/2}$	$1 \leqslant \Gamma \leqslant 6.2$
Prandtl number	$\text{Pr} \equiv \nu/\kappa$	$4.8 \lesssim Pr \lesssim 11$
Ekman number	$E \equiv \nu/(2\Omega h^2)$	$2.5 \times 10^{-6} \lesssim E \lesssim \infty$
Flux Rayleigh number	$R_f \equiv (\alpha_T g Q h^4)/(A\nu\kappa k)$	$8.8 \times 10^6 \lesssim R_f \lesssim 5.3 \times 10^{11}$
Rayleigh number	$\text{Ra} \equiv (\alpha_T g \Delta T h^3)/(\nu\kappa)$	$10^6 \lesssim \text{Ra} \lesssim 5.5 \times 10^9$
Nusselt number	$\text{Nu} \equiv (Qh)/(Ak\Delta T)$	$6.2 \lesssim \text{Nu} \lesssim 96.2$

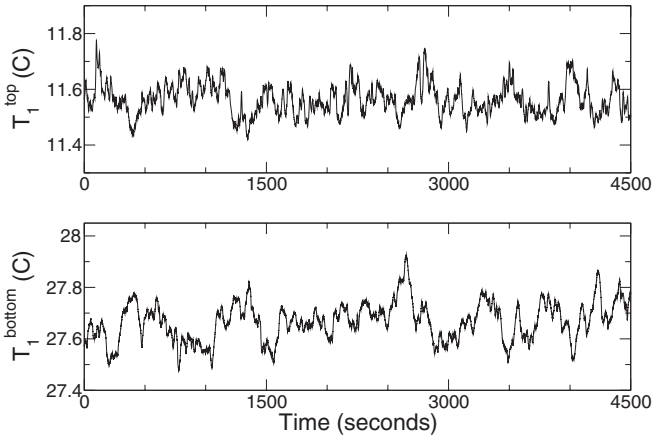

FIG. 3. An example of temperature time series data from a rotating RBC experiment ($R_f = 1.1 \times 10^{11}, E = 3 \times 10^{-6}$). The top panel shows measurements from a single thermistor in the top end wall [$T_1^{top}(t)$], and the bottom panel shows measurements from a thermistor below the fluid [$T_1^{bottom}(t)$].

and cold, downward flowing CTCs transport heat upward. Vertical conduits of heat such as CTCs will simultaneously cool the bottom boundary and warm the top boundary.

Negative correlations in temperature variations measured in the end walls therefore correspond to positive correlations in local vertical heat transport. As a control case, temperature correlations are calculated for thermistor pairs with both vertical and lateral separation. Discussed in detail in the Appendix, these horizontally separated temperature correlations produce significantly less coherent behavior than the purely vertically separated pairs for quasigeostrophic convection, in support of the interpretation of heat transfer by roughly vertical CTCs. This interpretation is further supported by a simple heat transfer model presented in Sec. IV.

Correlation data for weakly rotating and nonrotating convection are shown in Figs. 4(c) and 4(d). Both cases have $R_f = 1.1 \times 10^{11}$. The case shown in panel (c) has $E = 3 \times 10^{-5}$, and the data in panel (d) come from a nonrotating convection experiment. Temperature correlations in the absence of dominant rotation (panels c and d) produce different thermal signatures from quasigeostrophic convection (panels a and b). We observe broader, slightly positive correlation patterns in weakly and nonrotating convection experiments. This thermal signature is likely due to the development of large-scale circulations as the influence of rotation wanes.

Large-scale circulations have been found to produce positive thermal correlations in vertical thermistor pairs in nonrotating RBC experiments [e.g., [10]]. In contrast to heat transport by CTCs, large-scale circulations will typically produce vertically anticorrelated vertical heat flux and therefore positively correlated temperature signals within the boundaries. In other words, the thermal boundary layers are thickest where the large-scale circulation departs from the boundary [top left and bottom right corners of the cell depicted in Fig. 1(b)] and thinnest where it impinges (top right and bottom left). The right half of a counterclockwise large-scale circulation is anomalously warm, and the left half is cold, and so they produce positive vertical temperature correlations and negative horizontal temperature correlations, respectively [e.g., [28]].

We may therefore interpret positively correlated thermal signals as evidence for the development of large-scale circulations. In fact, visualizations in an uninsulated, nonrotating experiment with identical parameters as that shown in Fig. 4(d) confirm the existence of a large-scale circulation. The detailed dynamics of large-scale circulations are discussed elsewhere [e.g., [8,11,12]], and so we will not focus on this flow regime here. The inferred presence of these strongly three-dimensional flow patterns, however, indicates the breakdown of quasigeostrophic flow.

We should also note that the normalization used to calculate these correlations [Eq. (2)] inherently assumes that the different thermistors sample all parts of the large-scale circulation equally as the large-scale circulation wanders azimuthally [e.g., [11]]. If, however, the duration of experimental data acquisition were to be shorter than the time scale over which the large-scale circulation wanders, or if the large-scale circulation were to become locked in place, the cross correlation should be normalized not by each thermistor's time-averaged temperature but by the average of all thermistors on that level. Otherwise, we may be correlating small-scale plume behavior, instead of global dynamics. We have tried both normalizations, and find no appreciable change, indicating that we do, in fact, sample the large-scale circulation without such azimuthal bias.

In Fig. 5, we show the mean zero-lag vertical temperature correlation coefficient $\overline{C}$ for all experiments. These data are plotted against the transition parameter $\mathrm{Ra}E^{3/2}$, which is argued to separate quasigeostrophic and weakly rotating heat transfer regimes. In general, we observe anticorrelated signals in the quasigeostrophic regime (small $\mathrm{Ra}E^{3/2}$) and positively correlated signals in weakly (large $\mathrm{Ra}E^{3/2}$) and nonrotating ($E \approx \infty$) regimes. Negative correlations ($\overline{C} < 1$) are indicative of the importance of CTCs in transporting heat. Positive correlations ($\overline{C} > 1$) indicate the development of large-scale circulations.

IV. ONE-DIMENSIONAL CTC HEAT TRANSFER MODEL

In order to better understand the physical meaning of $C_i^{\mathrm{top-bottom}}$ in quasigeostrophic convection experiments, we examine a simple one-dimensional numerical model for vertical heat transport by CTCs. The model consists of a vertical profile of a fluid layer sandwiched between two end walls of finite thickness and thermal conductivity. As in the laboratory experiments, the temperature is fixed above the top end wall, and a heat flux is fixed below the bottom end wall. We model the drifting CTCs as a region of temporally fluctuating yet vertically uniform heat flux. This is accomplished by characterizing the convecting fluid as a solid thermal conductor with an effective conductivity $k_{\mathrm{eff}} = k_{\mathrm{fluid}}\mathrm{Nu}(t)$. Quantities used are accurate to material properties and experimental settings, and $\mathrm{Nu}(t)$ is generated artificially. We calculate the vertical temperature profile of the model at each time step, generating synthetic temperature time series within the model's top and bottom boundaries. The correlation coefficient can then be calculated as in the actual experiment. This simple model provides synthetic data for an end-member convection

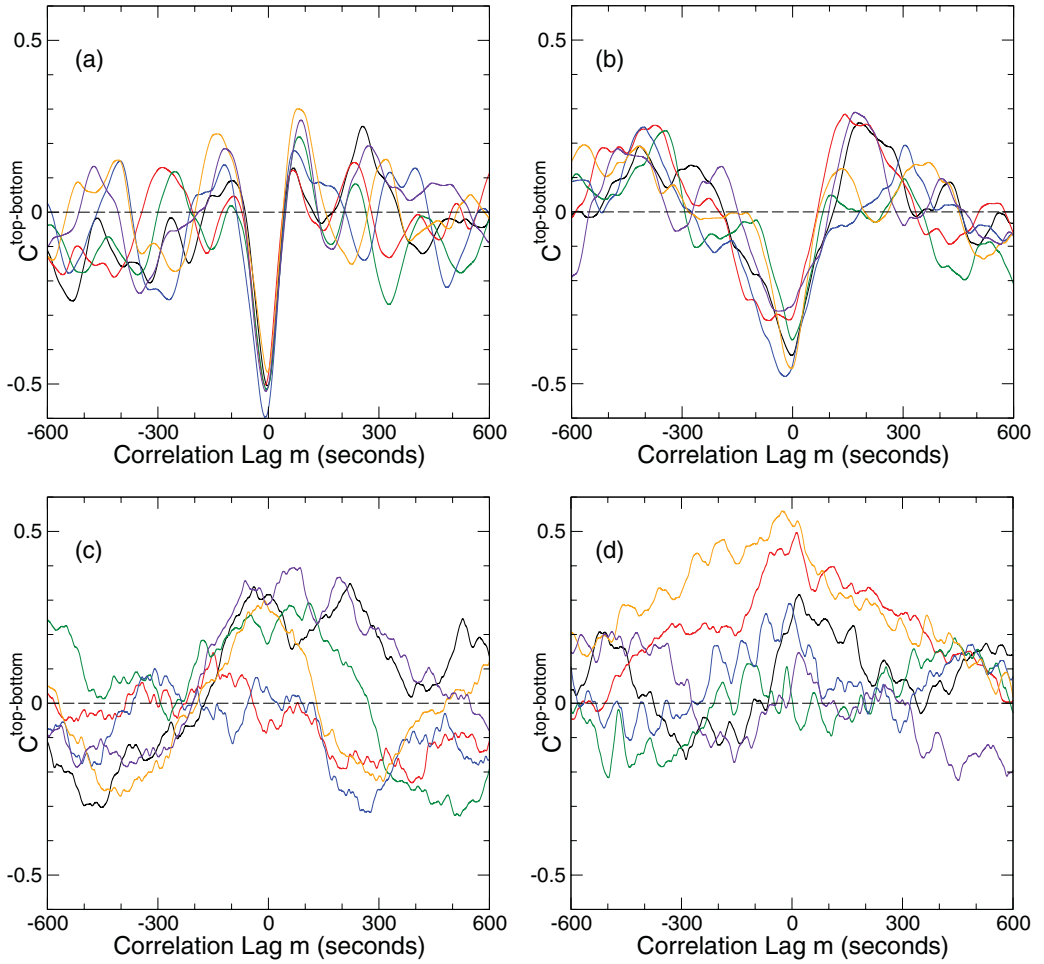

FIG. 4. (Color online) Temperature correlations from vertical thermistor pairs, $C_i^{\text{top-bottom}}$, vs correlation lag, $m \times dt$, as defined in Eq. (3). (a) $h = 4.7$ cm and $Q = 50$ W, and therefore $R_f = 2 \times 10^8$. (b–d) $h = 0.197$ m and $Q = 100$ W, and therefore $R_f = 1.1 \times 10^{11}$. (a) Rotating convection with $\Omega = 5.3$ Hz, $E = 4.4 \times 10^{-5}$, $\text{Ra}E^{3/2} \approx 5$. (b) Rotating convection with $\Omega = 4.3$ Hz, $E = 3 \times 10^{-6}$, $\text{Ra}E^{3/2} \approx 8$. (c) Rotating convection with $\Omega = 0.43$ Hz, $E = 3 \times 10^{-5}$, $\text{Ra}E^{3/2} \approx 280$. (d) Nonrotating convection.

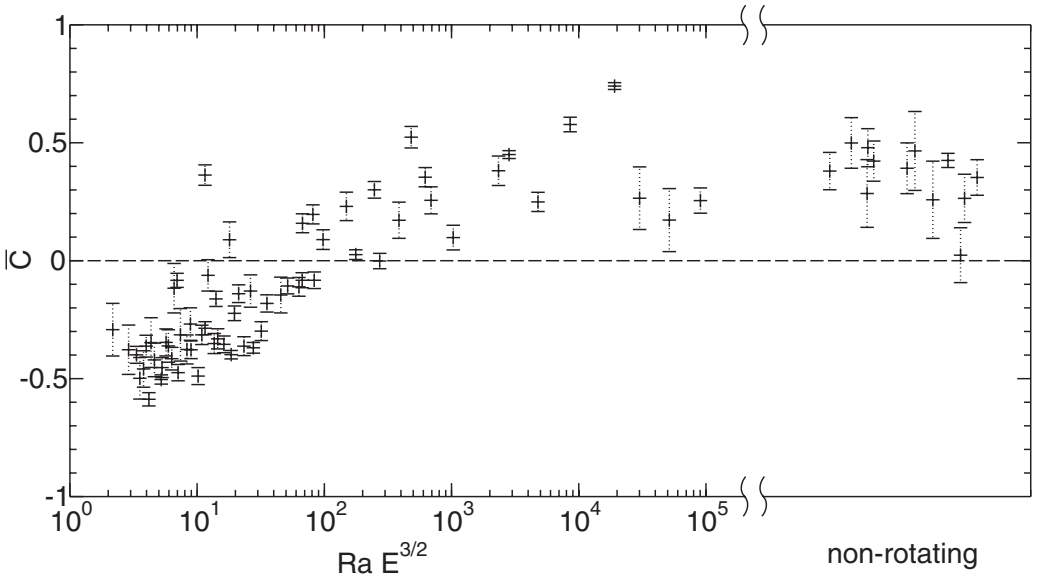

FIG. 5. Vertical temperature correlation coefficient at time lag $m = 0$ ($\overline{C}$) as defined in Eq. (2), vs $\text{Ra}E^{3/2}$. Error bars represent one standard deviation among the six thermistor pairs for each case. Rightmost data are from nonrotating experiments, for which the x coordinate is arbitrary.

scenario wherein heat is transferred entirely by space-filling, perfectly vertical CTCs. A more detailed description of the model is given below.

A. Model details

First, a one-dimensional model convection tank setup is constructed with dimensions to match the experiment, as shown in Fig. 6. The model consists of three layers (from bottom to top): a bottom end wall, which has thickness and thermal conductivity $h_{\text{bottom}} = 0.015$ m and $k_{\text{bottom}} = 390$ W/mK; a fluid layer with "tank" height h_{fluid} and $k_{\text{fluid}} = 0.6$ W/mK; and a top end wall with $h_{\text{top}} = 0.06$ m and $k_{\text{top}} = 167$ W/mK. The thermal boundary conditions are fixed in heat flux below the bottom tank end wall, $q = Q/A$, where A is the area through which the heat power Q is fluxed, and fixed in temperature above the top end wall, T^{cool}.

The basic idea of the model is to vary the efficiency of heat transfer in the fluid layer with time and solve for the temperature profile at each time step, t_i. We assume the convective heat transfer within the fluid is uniform in height, z, to approximate the behavior of an ideal CTC. This allows treatment of the fluid as a uniform material with effective thermal conductivity $k_{\text{eff}} = k_{\text{fluid}}\text{Nu}(t)$, where Nu is the Nusselt number. We use a time varying Nu to simulate a location in a three-dimensional fluid layer through which Taylor columns pass as they wander horizontally around the container.

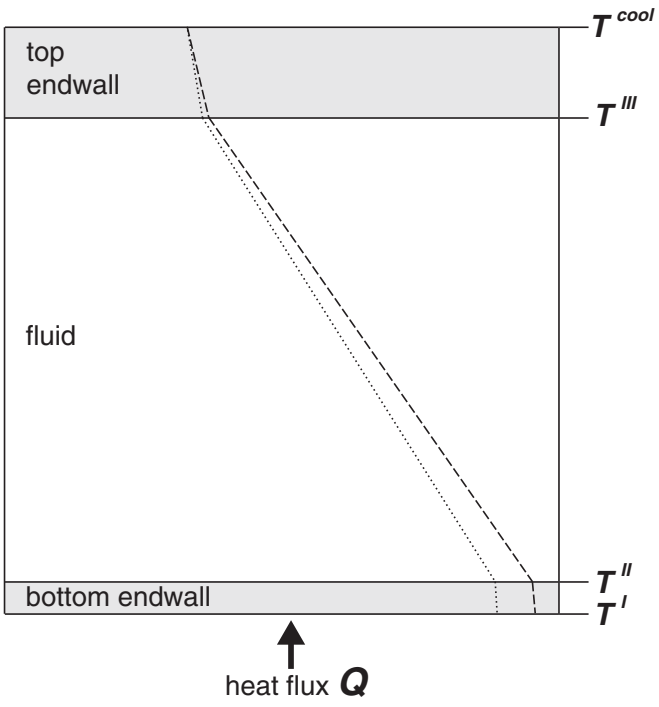

FIG. 6. A schematic illustration of the one-dimensional CTC heat transfer model. The three vertical layers, from bottom to top, are the bottom end wall, fluid layer, and top end wall. The vertical locations of the interfacial temperatures calculated in the model are denoted T^{I}, T^{II}, and T^{III}. The dotted and dashed lines illustrate instantaneous vertical temperature profiles generated by the model. The temperature gradient within the fluid layer varies with Nu(t).

Time series for Nu are synthesized using a modified random walk. Initially, $\text{Nu}(t = 0) = \text{Nu}_0$. For the remaining time steps $t_i = t_1, \ldots, t_{\text{max}}$, we generate $\text{Nu}(t_i) = \text{Nu}_i$ as follows:

$$\text{Nu}_i = \text{Nu}_{i-1} + C_1\left(R_1^i - 1/2\right) \quad \text{if} \quad \text{Nu}_{i-1} = \text{Nu}_0, \tag{4}$$

$$\text{Nu}_i = \text{Nu}_{i-1} + C_1\left(R_1^i - 1/2\right) - C_2 R_2^i \exp[-(\text{Nu}_0 - \text{Nu}_{i-1})/\text{Nu}_0] \quad \text{if } \text{Nu}_{i-1} > \text{Nu}_0, \tag{5}$$

$$\text{Nu}_i = \text{Nu}_{i-1} + C_1\left(R_1^i - 1/2\right) + C_2 R_2^i \exp[(\text{Nu}_0 - \text{Nu}_{i-1})/\text{Nu}_0] \quad \text{if } \text{Nu}_{i-1} < \text{Nu}_0, \tag{6}$$

where C_1 and C_2 are constants and R_1^i and R_2^i are numbers in the range $0 < R < 1$ generated randomly at each time step. The constant C_1 determines the typical variability of Nu between time steps ($\text{Nu}_i - \text{Nu}_{i-1}$). The third term in Eqs. (5) and (6) prescribes an exponentially weighted preference for Nu values to change in the direction of Nu_0. The constants C_1 and C_2 are positive and small, $0 < C < 1$, and are chosen such that the Nu time series is trendless about the desired value (Nu_0) and has statistical properties (e.g., variance and temporal power spectrum) similar to the actual experimental time series.

The temporal resolution of the model is set to match that of the acquisition frequency of experimental thermal measurements. We assume that the thermal diffusion time scale through the solid container boundaries is small compared to the typical time scale of fluctuations in convective heat transport. This assumption of instantaneous thermal equilibration allows us to solve for a thermally equilibrated temperature profile $T(z,t_i)$ at each time step. Based on visual observation of flow in nonrotating convection and estimates of convective free fall, advective time scales are expected to be tens of seconds to minutes in our experiments. The time scale for thermal diffusion over distance d is $\tau_\kappa \sim d^2\kappa$, where κ is the material's thermal diffusivity. Copper and aluminum have $\kappa = 1.1 \times 10^{-4}$ and 6.4×10^{-5}, respectively [29]. The time scale for diffusion between the fluid layer and thermistors is approximately 0.05 s, which is faster than both advective time scales and acquisition frequency. The time scale for diffusion across the entire top and bottom end walls is roughly 25 and 1.5 s, respectively. The diffusive time scale through the upper end wall, therefore, is not significantly faster than advective time scales. A more advanced model could include the influence of finite thermal diffusivity, but, since we've already drastically reduced the complexity of the true system with this toy model, we anticipate that this additional effect will not alter its fundamental result. Experimental and numerical examinations of the effects of finite conductivity boundaries are given in [30,31].

The heat flux and effective thermal conductivity are uniform in space within each layer, so the temperature will vary linearly in z within each layer, such that we need only solve for the temperatures at the interfaces between layers. The temperature above the top end wall is fixed at T^{cool}. The temperature between the top end wall and fluid is $T^{\text{III}}(t_i)$.

The temperature between the fluid and the bottom end wall is $T^{\mathrm{II}}(t_i)$. The temperature at the bottom of the lower end wall is $T^{\mathrm{I}}(t_i)$. The locations of these interfacial temperature calculations, $T^{\mathrm{I-III}}$, are shown in the schematic of Fig. 6. The aim of the model is to solve for these three temperatures at each time step t_i which depend on the predefined $\mathrm{Nu}(t_i)$.

Initially, we take

$$T^{\mathrm{III}}(t=0) = T^{\mathrm{cool}} + \frac{q\, h_{\mathrm{top}}}{k_{\mathrm{top}}}, \tag{7}$$

$$T^{\mathrm{II}}(t=0) = T^{\mathrm{III}} + \frac{q\, h_{\mathrm{fluid}}}{\mathrm{Nu}(t=0)\, k_{\mathrm{fluid}}}, \tag{8}$$

$$T^{\mathrm{I}}(t=0) = T^{\mathrm{II}} + \frac{q\, h_{\mathrm{bottom}}}{k_{\mathrm{bottom}}}. \tag{9}$$

For the remainder of the time steps, $t_1, \ldots, t_{\mathrm{max}}$, the temperatures are solved for as

$$T^{\mathrm{III}}(t_i) = T^{\mathrm{cool}} + \frac{\mathrm{Nu}(t_i)\, q\, h_{\mathrm{top}}}{\langle \mathrm{Nu} \rangle\, k_{\mathrm{top}}}, \tag{10}$$

$$T^{\mathrm{II}}(t_i) = T^{\mathrm{III}} + \frac{q\, h_{\mathrm{fluid}}}{\mathrm{Nu}(t_i)\, k_{\mathrm{fluid}}}, \tag{11}$$

$$T^{\mathrm{I}}(t_i) = T^{\mathrm{II}} + \frac{q\, h_{\mathrm{bottom}}}{k_{\mathrm{bottom}}}. \tag{12}$$

Notice that the temperature above the fluid, $T^{\mathrm{III}}(t_i)$, is dependent on fluctuations of Nu about its mean $\langle \mathrm{Nu} \rangle \approx \mathrm{Nu}_0$. This is due to the convecting fluid's control of how much of the base heating q reaches the top end wall, as the fluid acts as a heat flux capacitor.

Once the temperature profile time series are generated, it is possible to extract a synthetic thermistor time series measurement. In the experiment, the thermistors are located within the end walls, 2 mm from the fluid boundary. Synthetic top and bottom thermistor data are then

$$T^{\mathrm{top}}(t_i) = T^{\mathrm{III}}(t_i) - \left(\frac{0.002\,\mathrm{m}}{h_{\mathrm{top}}}\right)[T^{\mathrm{III}}(t_i) - T^{\mathrm{cool}}], \tag{13}$$

$$T^{\mathrm{bottom}}(t_i) = T^{\mathrm{II}}(t_i) + \left(\frac{0.002\,\mathrm{m}}{h_{\mathrm{bottom}}}\right)[T^{\mathrm{II}}(t_i) - T^{\mathrm{II}}(t_i)]. \tag{14}$$

Examples of these synthetic thermistor data are shown in Fig. 7 and can be compared directly to experimental data (Fig. 3). Note that the top temperature shows much smaller variance than both the bottom temperature as well as the top temperature from actual experiments. This is likely due to the assumption of instantaneous thermal equilibration, which will smooth vertical variations and limit their amplitude. The absolute amplitudes of variations, however, are not important for normalized cross-correlation coefficients, which are calculated for the synthetic data exactly as in actual experiments using Eq. (2).

B. Model results

Figure 8 shows calculations of vertical correlations, $C_i^{\mathrm{top-bottom}}$, from six model iterations. The model parameters are set to $h_{\mathrm{bottom}} = 0.015$ m, $k_{\mathrm{bottom}} = 390$ W/mK, $h_{\mathrm{fluid}} = 0.197$ m, $k_{\mathrm{fluid}} = 0.6$ W/mK, $h_{\mathrm{top}} = 0.06$ m, $k_{\mathrm{top}} = 167$ W/mK, $Q = 100$ W, $T^{\mathrm{cool}} = 10$ C, $t_{\mathrm{max}} = 3000$ s, $\mathrm{Nu}_0 = 66$, $C_1 = 0.01$, and $C_2 = 0.0004$. These values are chosen in order to simulate the experimental setting from which the data in Figs. 3 and 4(a) are collected.

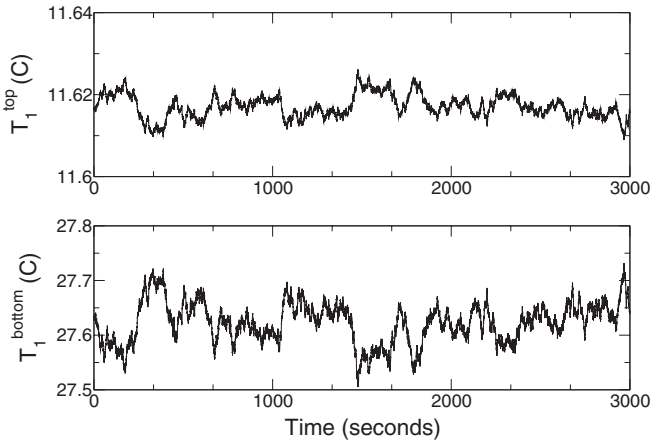

FIG. 7. An example of synthesized temperature time series data produced by the one-dimensional CTC heat transfer model. The top panel shows synthetic measurements in the top end wall $[T_1^{\mathrm{top}}(t)]$, and the bottom panel shows data from the lower end wall $[T_1^{\mathrm{bottom}}(t)]$. Model parameters are $h_{\mathrm{fluid}} = 0.197$ m, $Q = 100$ W, $T^{\mathrm{cool}} = 10$ C, and $\mathrm{Nu}_0 = 66$. Compare with experimental data shown in Fig. 3.

At zero time lag (m = 0), the correlation is perfect ($|\overline{C}| = 1$), owing to the assumption of perfectly uniform, vertical heat transport at each time step. The sign of the correlation, however, is negative, in agreement with the thermal anticorrelations observed experimentally [Figs. 4(a) and 4(b)].

The nature of the time series used for $\mathrm{Nu}(t)$ is unimportant for producing anticorrelated temperature calculations at zero

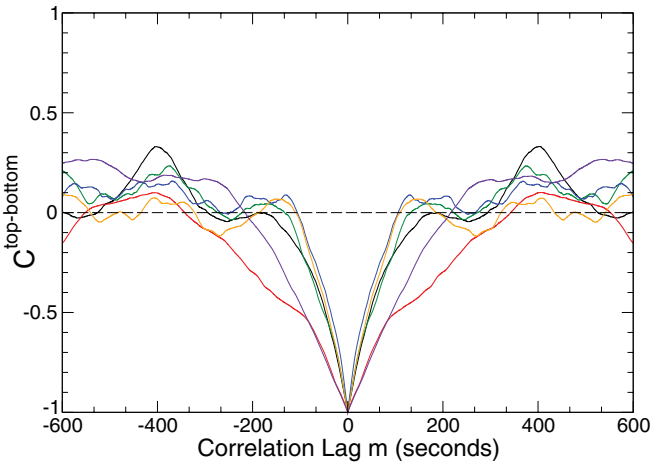

FIG. 8. (Color online) Temperature correlations calculated from synthetic thermistor data from the one-dimensional CTC heat transfer model. Model parameters are $h_{\mathrm{fluid}} = 0.197$ m, $Q = 100$ W, $T^{\mathrm{cool}} = 10$ C, and $\mathrm{Nu}_0 = 66$. Six separate model results are shown, wherein different Nu time series are used in order to approximate the six different thermistor pairs used in actual experiments. Instantaneous temperature values within the top and bottom end walls are strongly anticorrelated.

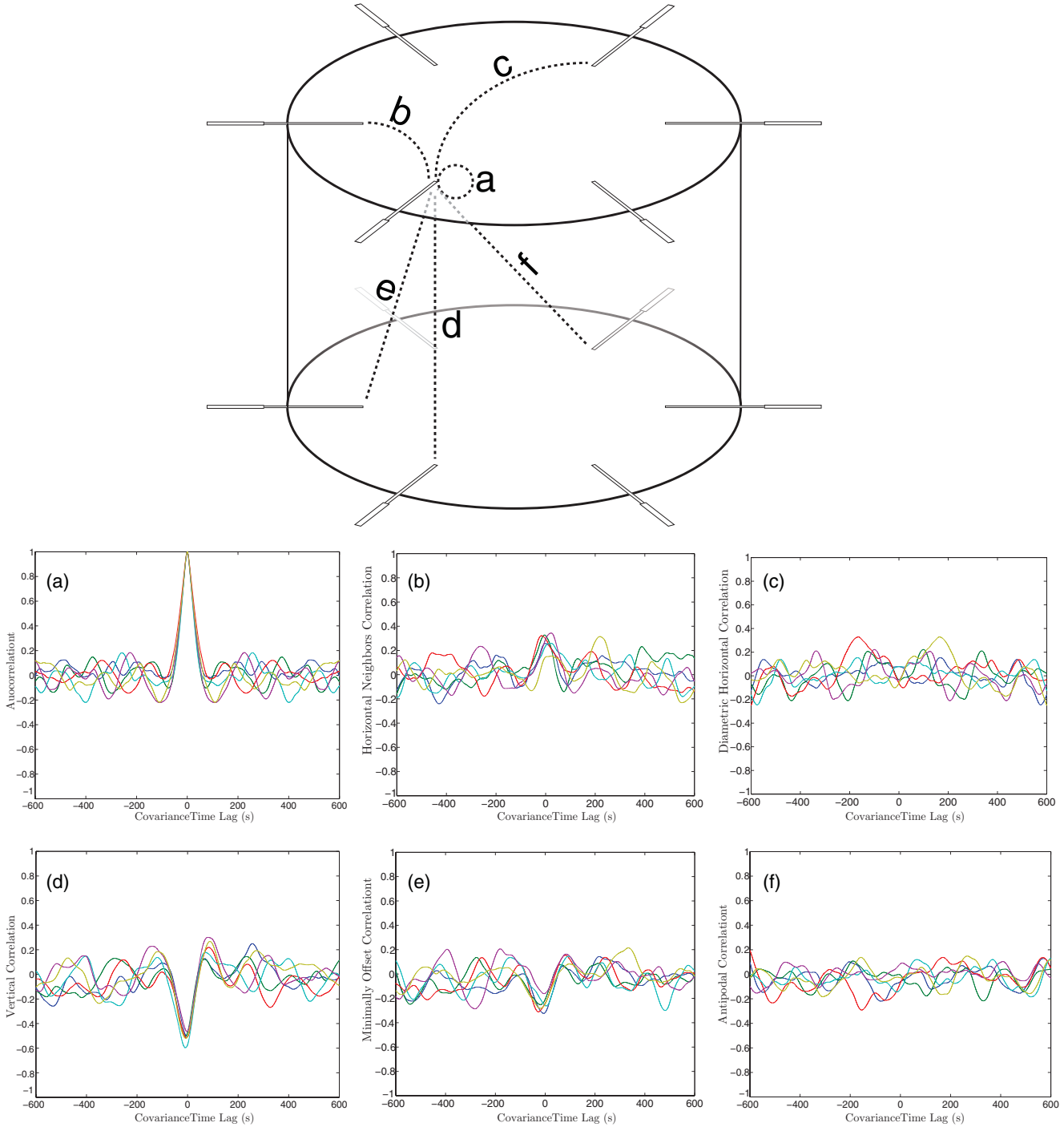

FIG. 9. (Color online) Temperature correlations from a geostrophic convection experiment plotted vs correlation lag for six types of thermistor pairs: (a) autocorrelation of the thermistor signal with itself, (b) horizontal pairs of nearest neighbors, (c) horizontal pairs of diametrically opposed thermistors, (d) vertically aligned and vertically separated thermistors (our original analysis), (e) minimally laterally offset and vertically separated thermistors, and (f) maximally laterally separated and vertically separated (antipodal) pairs. The experimental case shown has $h = 4.7$ cm, $Q = 50$ W, and $\Omega = 5.3$ Hz, and therefore $R_f = 2 \times 10^8$, $E = 4.4 \times 10^{-5}$, $\mathrm{Ra}E^{3/2} \approx 5$. Panel (d) is identical to Fig. 4(a).

lag. If $\mathrm{Nu}(t)$ varies as white noise, for example, we again find a perfect anticorrelation at $m = 0$. But, since each value in a white time series is independent of the previous value, $C(m \neq 0) = 0$ over an ensemble average. In order to produce correlation profiles with broader ranges of nonzero values, the time series must have nonzero autocorrelation. The width of the troughs observed in Figs. 4(a), 4(b), and 8 are therefore linked to the spectral properties of the time series, which is in turn linked to the convective flow. We leave a detailed analysis of temporal spectra for future work.

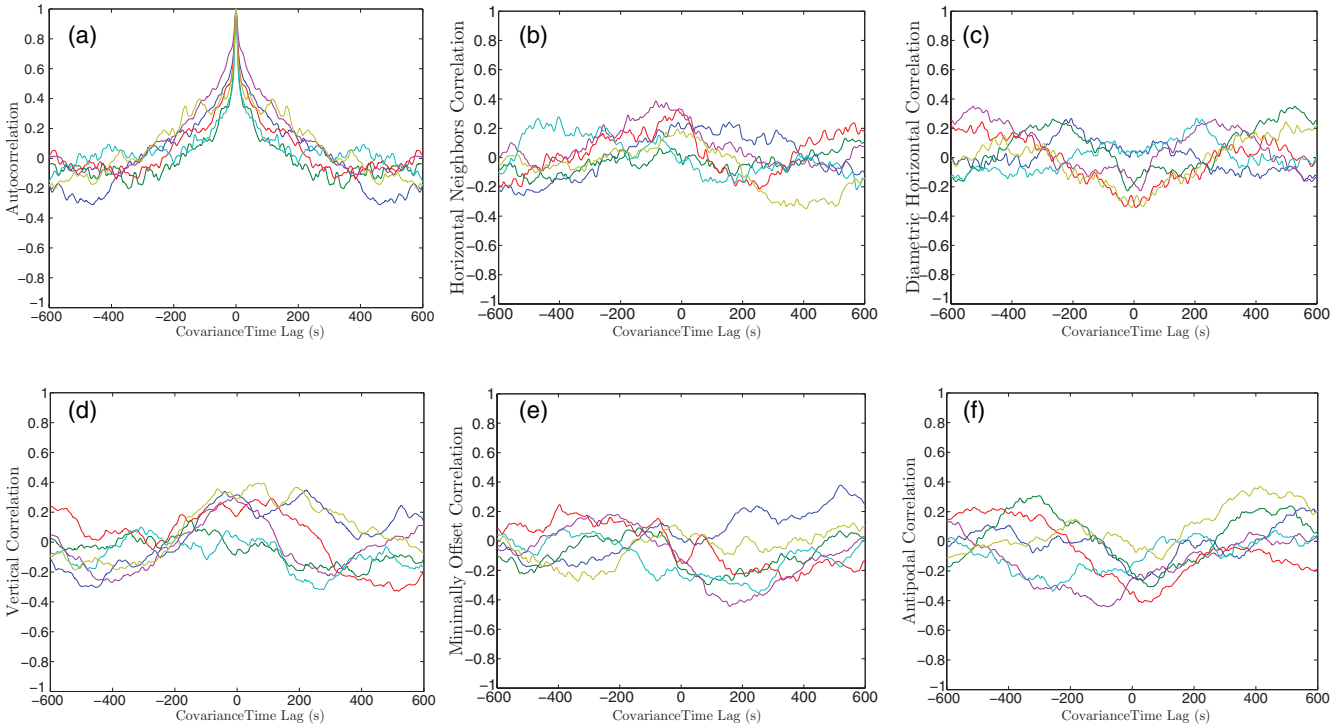

FIG. 10. (Color online) Vertically and/or horizontally separated temperature correlations from a weakly rotating convection experiment plotted vs correlation lag. As in Fig. 9, the six types of thermistor pairs are (a) autocorrelation of the thermistor signal with itself, (b) horizontal pairs of nearest neighbors, (c) horizontal pairs of diametrically opposed thermistors, (d) vertically aligned and vertically separated thermistors (our original analysis), (e) minimally laterally offset and vertically separated thermistors, and (f) maximally laterally separated and vertically separated (antipodal) pairs. The experimental case shown has $h = 19.7$ cm, $Q = 100$ W, and $\Omega = 0.43$ Hz, and therefore $R_f = 1 \times 10^{11}$, $E = 3 \times 10^{-5}$, $\mathrm{Ra}E^{3/2} \approx 280$. Panel (d) is identical to Fig. 4(c).

V. DISCUSSION

Figures 1(c) and 4(b) both show results from rapidly rotating, turbulent Rayleigh-Bénard convection with $R_f = 1.1 \times 10^{11}$ and $E = 3 \times 10^{-6}$. Figure 8 shows synthetic data from an idealized model of heat transport by Taylor columns with parameters set to simulate these experiments. The qualitative agreement between experimental correlation measurements and the synthetic model data supports the idea that anticorrelated temperature measurements are indicative of the presence of CTCs. That the model data have a much stronger anticorrelation is due to the assumption of perfectly uniform, perfectly vertical instantaneous heat transport at all times. Possible causes for imperfect correlation ($|\overline{C}| < 1$) in experiments include lateral diffusion of heat in CTCs and end walls, diffusive heat transport in the space between CTC cores, and the fact that CTCs may not be perfectly vertical and container high. Flow visualizations [Fig. 1(c)], however, further verify the columnar nature of flow in experiments with identical parameters to those that produce vertically anticorrelated temperature signals [Fig. 4(b)]. The general agreement between these three figures indicates that convection within this regime is manifest as tall, roughly vertical, thermally active CTCs.

Reference [25] shows that the thermal boundary layer is thinner than the Ekman boundary layer when $\mathrm{Ra}E^{3/2} \gtrsim 20$ in rotating RBC simulations. This transition also corresponds to a change in heat transfer behavior from quasigeostrophic to weakly rotating. Here, we observe that some experiments with $20 < \mathrm{Ra}E^{3/2} \lesssim 100$ produce anticorrelated signals. From this we infer that when the thermal boundary layer thickness is smaller than but comparable to the Ekman boundary layer thickness, CTCs can still exist. This contention is in agreement with the idea that the intensification of heat transfer observed near this transition is related to Ekman pumping in the presence of a thermal boundary layer [32]. The scatter in experimental $\overline{C}$ data precludes the identification of any clear transition point between quasigeostrophic CTCs and weakly rotating large-scale circulation. This difficulty remains regardless of the abscissa parameter chosen in Fig. 5 [including, for example, the convective Rossby number, $\mathrm{Ro}_c = (\mathrm{Ra}E^2/\mathrm{Pr})^{1/2}$].

To summarize, we find two rotating convective regimes, termed quasigeostrophic and weakly rotating. In quasigeostrophic convection, heat is transported by tall, thin, vertical conduits known as convective Taylor columns. These flow structures wander about horizontally, pumping warm fluid from bottom to top or vice versa. Locally, this flow (nearly) simultaneously cools the bottom boundary and warms the top boundary due to their finite conductivity and therefore produces anticorrelated vertical temperature signatures. In the weakly rotating regime, large-scale circulations produce warm and cool "piles" of material that generate positively correlated vertical temperature signatures.

It remains unclear over what range of parameters CTCs are stable. The width of a CTC should scale as $E^{1/3}$ [33]. As E decreases to the very low values predicted in planetary

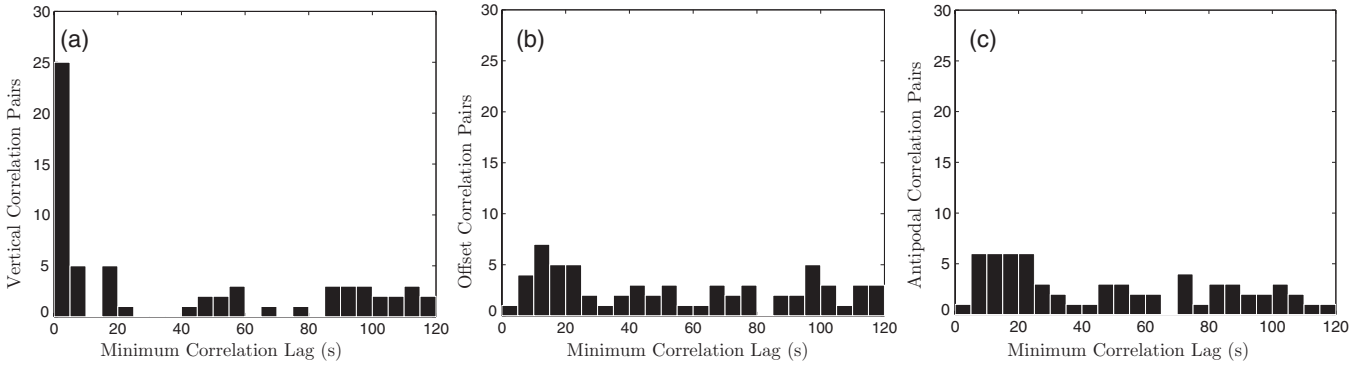

FIG. 11. Histograms of the time lags at which vertically separated thermistor pairs produce maximum anticorrelations for geostrophic experiments ($\mathrm{Ra}E^{3/2} < 10$). Panel (a) shows data from thermistor pairs with no lateral separation. Panel (b) shows data from minimally laterally offset pairs. Panel (c) shows antipodal (maximally offset) pairs.

settings, CTCs become increasing thin and may undergo instabilities [34]. Furthermore, in low-Pr fluids such as liquid metals, the thermal anomalies carried in CTCs may be more effectively diffused, and so the columns may not extend across the layer. As an example, the observation of two pairs of geomagnetic flux patches that are nearly symmetric about the equator evokes, as an explanation, the existence of CTCs in Earth's field-generating core [e.g., [35,36]]. Earth's liquid metal outer core has $E \approx 10^{-15}$ and $\mathrm{Pr} \lesssim 0.1$, and it is not clear that large-scale CTCs can exist in such an extreme setting. We can answer these questions by looking for evidence of CTCs in experiments with increasingly extreme parameters.

ACKNOWLEDGMENTS

E.M.K acknowledges the support of the Miller Institute for Basic Research in Science. J.M.A was funded by the NSF Geophysics Program (No. EAR-0944312) and the NASA Planetary Atmospheres Program (No. NNX09AB61G).

APPENDIX

To serve as a control group for the conclusions drawn from the correlation data shown in Fig. 4, we have calculated correlations between thermistor pairs with both vertical and lateral separation. We look at correlations with two types of lateral separation: either azimuthal neighbors (minimally offset), with 7-cm lateral separation, or maximally separated diametrically opposed pairs (antipodal), separated by 13 cm laterally. For quasigeostrophic experiments, some of these pairs do still produce negative correlations, but these are always weaker than the correlations between purely vertical thermistors and grow weaker with increasing lateral separation.

Figure 9 shows a comparison of correlation coefficients for six types of thermistor pairs: (a) autocorrelation of the thermistor signal with itself; (b) horizontal pairs of nearest neighbors; (c) horizontal pairs of diametrically opposed thermistors; (d) vertically aligned and vertically separated thermistors (our original analysis); (e) minimally laterally offset and vertically separated thermistors; and (f) maximally laterally separated and vertically separated (antipodal) pairs. The experimental case shown is the same as in Fig. 4(a), which is in the geostrophic regime ($\mathrm{Ra}E^{3/2} \approx 5$). These geostrophic correlations become less coherent as lateral separation is increased.

Figure 10 shows a comparison of correlation coefficients for the six types of thermistor pairs, as shown in Fig. 9, but now for the weakly rotating convection experiment data shown in Fig. 4(c). The correlations are weak in general. We do notice that the weak positive correlations seen in the purely vertically separated pair are complemented by weakly anticorrelated signals for the antipodal pairs. This fits with our interpretation of these thermal signatures as being produced by large-scale circulations, which should produce heat flux anomalies that are anomalously high in the tank corners that are antipodally opposed.

We can test the CTC interpretation of the temperature correlations more systematically by determining the time lag at which vertical correlations are maximally anticorrelated in the geostrophic experiments. Heat transfer by wandering CTCs should result in maximum anticorrelations at lag ($k \approx 0$) for the vertically aligned thermistor pairs, but should show no strong bias in lag space for the horizontally separated pairs. We calculate the lag at which the correlation coefficient is minimal (within a 10-min lag range) for each pair for the 64 cases with $\mathrm{Ra}E^{3/2} < 10$. Figure 11 shows a histogram of the results of this calculation. For the pairs with purely vertical separation (a), there is a strong likelihood that geostrophic convection will produce minimum correlation (maximum anticorrelation) near $k = 0$. For pairs with lateral separation (b and c), this strong preference disappears. This supports our argument that the anticorrelations observed in vertical pairs for geostrophic convection are due to wandering Taylor columns.

[1] G. I. Taylor, Proc. R. Soc. London A **100**, 114 (1921).
[2] K. Julien and E. Knobloch, Phys. Fluids **11**, 1469 (1999).
[3] G. Veronis, J. Fluid Mech. **5**, 401 (1959).
[4] M. Sprague, K. Julien, E. Knobloch, and J. Werne, J. Fluid Mech. **551**, 141 (2006).

[5] J. McWilliams, *Fundamentals of Geophysical Fluid Dynamics* (Cambridge University Press, Cambridge, UK, 2006).
[6] S. Sakai, J. Fluid Mech. **333**, 85 (1997).
[7] E. King, S. Stellmach, J. Noir, U. Hansen, and J. Aurnou, Nature (London) **457**, 301 (2009).
[8] J. Hart, S. Kittelman, and D. Ohlsen, Phys. Fluids **14**, 995 (2002).
[9] J.-Q. Zhong and G. Ahlers, J. Fluid Mech. **665**, 300 (2010).
[10] S. Cioni, S. Ciliberto, and J. Sommeria, J. Fluid Mech. **335**, 111 (1997).
[11] E. Brown and G. Ahlers, Phys. Rev. Lett. **98**, 134501 (2007).
[12] H. Xi, S. Lam, and K. Xia, J. Fluid Mech. **503**, 47 (2004).
[13] H. Rossby, J. Fluid Mech. **36**, 309 (1969).
[14] K. Julien, S. Legg, J. McWilliams, and J. Werne, J. Fluid Mech. **322**, 243 (1996).
[15] Y. Liu and R. E. Ecke, Phys. Rev. Lett. **79**, 2257 (1997).
[16] J. Aurnou, Geophys. Astrophys. Fluid Dyn. **101**, 327 (2007).
[17] Y. Liu and R. Ecke, Phys. Rev. E **80**, 6314 (2009).
[18] J. Q. Zhong, R. J. A. M. Stevens, H. J. H. Clercx, R. Verzicco, D. Lohse, and G. Ahlers, Phys. Rev. Lett. **102**, 044502 (2009).
[19] E. King, K. Soderlund, U. R. Christensen, J. Wicht, and J. M. Aurnou, Geochemistry Geophysics Geosystems **11**, Q06016 (2010).
[20] J. J. Niemela, S. Babuin, and K. R. Sreenivasan, J. Fluid Mech. **649**, 509 (2010).
[21] S. Schmitz and A. Tilgner, Phys. Rev. E **80**, 5305 (2009).
[22] S. Schmitz and A. Tilgner, Geophys. Astrophys. Fluid Dyn. **104**, 1 (2010).
[23] B. Boubnov and G. Golitsyn, J. Fluid Mech. **219**, 215 (1990).
[24] E. M. King, Ph.D. thesis, University of California, Los Angeles, 2009.
[25] E. M. King, S. Stellmach, and J. M. Aurnou, J. Fluid Mech. **691**, 568 (2012).
[26] J. Noir, D. Brito, K. Aldridge, and P. Cardin, Geophys. Res. Lett. **28**, 3785 (2001).
[27] D. Hathaway, Astrophys. J. **276**, 316 (1984).
[28] J. J. Niemela and K. R. Sreenivasan, J. Fluid Mech. **557**, 411 (2006).
[29] D. R. Lide, *Handbook of Chemistry and Physics* (CRC, Boca Raton, 2000).
[30] E. Brown, A. Nikolaenko, D. Funfschilling, and G. Ahlers, Phys. Fluids **17**, 075108 (2005).
[31] R. Verzicco, Phys. Fluids **16**, 1965 (2004).
[32] R. J. A. M. Stevens, H. J. H. Clercx, and D. Lohse, Phys. Fluids **22**, 085103 (2010).
[33] S. Chandrasekhar, *Hydrodynamic and Hydromagnetic Stability* (Dover, New York, 1961).
[34] P. Billant, J. Fluid Mech. **660**, 354 (2010).
[35] D. Gubbins and J. Bloxham, Nature (London) **325**, 509 (1987).
[36] P. Olson, U. Christensen, and G. Glatzmaier, J. Geophys. Res. **104**, 10383 (1999).